NUMERICAL SIMULATION OF OBLIQUE OSCILLATORY FLOW OVER BED RIPPLES USING THE IMMERSED BOUNDARY METHOD

Iason A. Chalmoukis[1] and Athanassios A. Dimas[1]

[1]Department of Civil Engineering
University of Patras
Rio Patras, GR-26400, Greece
e-mail: ichalmoukis@upatras.gr, adimas@upatras.gr

Keywords: Immersed boundary, 3-dimensional analysis, ripples, oscillatory flow.

Abstract. *The objective of this paper is to simulate the three-dimensional flow induced by an oblique oscillatory flow over bed ripples. The discretization of the Navier-Stokes equations is done on a Cartesian grid, where the bed surface is an interface immersed in the numerical grid, following the immersed boundary method. The spatial discretization is based on the use of finite differences on a staggered grid for the dependent variables, and a two-stage time-splitting method is employed for the velocity-pressure coupling. To validate the accuracy, results for two-dimensional oscillatory flow were compared to previous numerical simulation and good agreement is found. For this case, the dimensions of the ripple are $L_r/a_o = 1.333$, $h_r/a_o = 0.2$, and the Reynolds number is $Re = 1250$, where L_r is the ripple length, a_o is the orbital motion amplitude and h_r is the ripple height. In the present study, three cases of ripple dimensions were examined, $L_r/a_o = 1.647$ and $h_r/a_o = 0.231$, $L_r/a_o = 1.445$ and $h_r/a_o = 0.205$ and $L_r/a_o = 0.991$ and $h_r/a_o = 0.136$, with $Re = 1250$. Also, two cases of flow direction were studied; one perpendicular and one at an angle of 45^o to the ripple crestline. Results show that the largest ripples produce stronger vortices. In addition, the y-velocity component of the oblique flow is important on the formation of the vorticity field.*

1 INTRODUCTION

Surface waves in the coastal zone induce oscillatory flow motions in the vicinity of the seabed. These motions interact with the bottom sediment and modify the bed shape by generating coherent structures, which are generally known as sand ripples. These ripples have usually a sharp crest and a symmetric shape with respect to the crest due to the oscillatory nature of the boundary layer flow induced by the propagation of waves. A typical ripple is shown in Fig. 4, where L_r is its length and h_r is its height. Ripple dimensions are associated with the parameters of the oscillatory flow that generated them, and according to field and experimental data, it has been reported that $L_r/a_o \lessapprox 2.2$ and $h_r/L_r \lessapprox 0.2$ ([6]; [13]; [8]).

The presence of a rippled bed in oscillatory flows modifies the development of the wave boundary layer and the propagation of water waves in comparison to a flat bed, because of flow separation and vortex shedding at the ripple crest. In coastal engineering applications, the influence of these flow phenomena on parameters associated with sediment transport close to the bed, i.e., wall stress, bed resistance, and time-averaged velocity, is of particular interest.

Experiments with ripples under oscillatory flow date back to the end of the 19th and the beginning of the 20th century, but it was not until the late 1950s that large-scale studies took place. The size of the facilities in more recent laboratory experiments has increased significantly compared to earlier works, as well as the quality and quantity of the data obtained, e.g. at Large Oscillating Water Tunnel (LOWT) at WL|Delft Hydraulics ([12]; [10]; [1]).

Concerning the numerical simulations, several computational studies have been reported in the literature, simulating the flow over fixed ripples, in an effort to understand the effects of such complex bed forms on the flow field and the evolution of the suspended sediment.

Malarkey and Davies studied numerically the oscillatory flow over ripples for $0.5 \leq L_r/a_o \leq 2$ and $0.13 \leq h_r/L_r \leq 0.2$, utilizing a discrete vortex method to explore the behavior of the eddy viscosity and concluded that the thickness of the resulting oscillating boundary layer is considerably larger than the one over a flat bed [5]. Scandura et al. studied numerically the viscous, three-dimensional instability and vorticity dynamics of oscillatory flow over two-dimensional ripples with smooth crests. In particular, for $R = 1.005$, $L_r/a_o = 1.33$ and $h_r/L_r = 0.14$, they showed that vortex shedding at the ripples' crests becomes three-dimensional and forms vorticity streaks that eject vorticity upward [11]. Barr et al. studied numerically the turbulent, three-dimensional oscillatory flow over two-dimensional ripples with smooth crests and profiles of increasing steepness for $R =$

15.600, Lr/α_o = 1.28 and h_r/ L_r = 0.18 and concluded that the wave boundary layer thickness over rippled bed increases, while the average wall shear stress decreases with increasing ripple profile steepness [3].

As it is mentioned above, during the past, several numerical simulations were carried out for a perpendicular flow over a rippled bed. In the present study, the focus has been extended to the oblique oscillatory flow. The scope of this paper is to simulate the three-dimensional flow induced by an oblique oscillatory flow over bed ripples by means of an advanced Navier-Stokes solver. The discretization of the Navier-Stokes equations is done on a Cartesian grid where the bed surface is an interface immersed in the numerical grid, following the immersed boundary (IB) method [2]. As a result, the implementation of the boundary conditions is achieved through additional terms, which are introduced in the momentum equations at the nodes closest to the boundaries (these are called forcing points). The spatial discretization is based on the use of finite differences on a staggered grid for the dependent variables (u, v, w, p), and a two-stage time-splitting method is employed for the velocity-pressure coupling.

The primary objective is to study the effect of the oblique oscillatory flow over a rippled bed on the vorticity dynamics and the velocity field. A brief description of the methodology is presented in the next session, followed by the results and conclusions.

2 METHODOLOGY

2.1 Mathematical and numerical implementation

The governing flow equations are the continuity

$$\frac{\partial u_i}{\partial x_i} = 0 \tag{1}$$

and the Navier-Stokes equations

$$\frac{\partial u_i}{\partial t} + \frac{\partial}{\partial x_j}\left(u_i u_j\right) = -\frac{\partial p}{\partial x_i} + \frac{1}{\mathrm{Re}}\frac{\partial^2 u_i}{\partial x_j \partial x_j} + f_i \tag{2}$$

where u_i are the velocity components, t is the time, x_i are the coordinates, p is the dynamic pressure, Re is the Reynolds number and f_i represents a source term associated with the implementation of the IB method for the enforcement of non-slip boundary conditions on the immersed bed surface. The dynamic pressure is split according to the expression:

$$p = P + \delta P \tag{3}$$

into the dynamic pressure P of the external flow, and the dynamic pressure correction δP due to the presence of immersed solid bodies.

The spatial discretization of the governing equations is based on the use of finite differences on a Cartesian staggered grid where velocity components are calculated at the center of the cube sides while pressure is calculated at the cube center (Fig. 1).

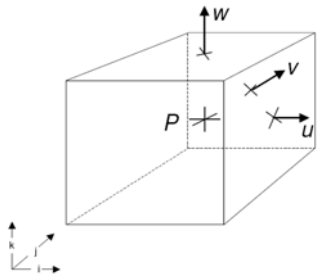

Figure 1. Cartesian staggered grid

The Navier-Stokes equations are discretized through a two-stage, time-splitting scheme, where an intermediate velocity is computed explicitly without, however, taking into account the pressure;

$$\frac{\hat{u}_i - u_i^n}{\Delta t} = H\left(u_i^n\right) + \frac{\partial P^{n+1}}{\partial x_i} + f_i^{n+1} \tag{4}$$

where H is a spatial operator, including the convective and viscous terms, and P is the dynamic pressure of the external flow.

The pressure gradient is obtained by solving the Poisson equation for the total pressure that is derived by enforcing the continuity constraint.

$$\frac{\partial^2 \delta P}{\partial x_i \partial x_i} = -\frac{1}{\Delta t}\frac{\partial \hat{u}_j}{\partial x_j} \tag{5}$$

The left hand side of the Poisson equation is composed by a seven-diagonal matrix. The solving of the matrix is implemented through an LU decomposition [4]. The boundary conditions that are imposed to the computational domain are: Dirichlet for the bottom, rigid lid for the top, and periodicity exists along the x and y direction.

Finally, the computation of the velocity at the next time-step is expressed by:

$$u_i^{n+1} = \hat{u}_i - \Delta t \frac{\partial \delta P}{\partial x_i} \tag{6}$$

2.2 Immersed boundary method

For the introduction of the rippled bed in the computational domain, which is discretized with a structured Cartesian grid, the IB method is utilized. The method, which was initially developed by [9], is explained in detail in [2]. The main characteristic of the implementation of the IB method in the present study is that the bed surface is not aligned with the grid. In such cases, the solution is reconstructed, in the vicinity of the boundary, in order to enforce the no-slip conditions.

Every wall surface within the computational domain is discretized using marker points with spacing approximately equal to the local grid size. For each boundary, an arclength coordinate s is defined so that the fluid is always to the left in the direction of increasing s. For each marker point, polynomial functions are defined by the expressions:

$$\begin{aligned} x_1(s) &= a_1 s^2 + b_1 s + c_1 \\ x_2(s) &= a_2 s^2 + b_2 s + c_2 \end{aligned} \tag{7}$$

where the coefficients α, b and c are computed by fitting the polynomial functions to the marker point i_b and its neighbours (i_b -1) and (i_b +1). Thus, the unit normal vector from any boundary point to the fluid can be computed directly through:

$$n_1 = \frac{-x_{2S}}{\sqrt{x_{1S}^2 + x_{2S}^2}} \qquad n_2 = \frac{x_{1S}}{\sqrt{x_{1S}^2 + x_{2S}^2}} \tag{8}$$

where index s denotes the derivative operation according to Eq. (7).

Next, for each marker point x_b, the closest grid point with coordinates x_i is identified. The points of the 3×3 group around x_i are defined as the points in the vicinity of the marker point. For each of the 3×3 points, the coordinates x_n of their projection on the immersed boundary are computed as the intersection between the line $x_2=(-1/\alpha_1)x_1+d$, which is normal to the immersed boundary (Fig. 2), and the polynomial expressions (Eq. 7). The resulting system of equations for the coordinates x_n is solved using a Newton-Raphson method. Then, the scalar product $\sigma=n_i \lambda_i$ is evaluated, where λ_i is the unit vector in the direction from the grid point x_i to the boundary point x_n, and n_i is the unit normal vector of Eq. (8). If σ = 1 the point belongs to solid phase, and if σ = -1 to fluid phase. The scalar σ is the phase flag of all grid points in the vicinity of the immersed boundary, and all the other grid points have σ = 0. Finally, through a search process, all grid points in the fluid phase that have at least one neighbor (in their 3×3 neighborhood) in the solid phase retain their flag value, and are identified as the forcing points. All the other points in the domain get a zero flag value. The forcing points are the ones where the boundary conditions of the immersed boundary will be enforced by projection.

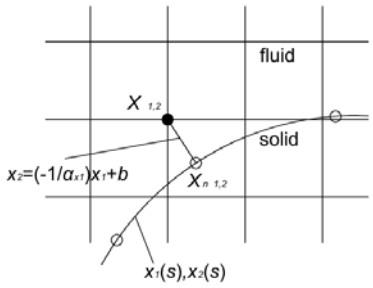

Figure 2. Definition of interface point normal to a grid point as intersection of two lines

The above methodology gives the indices (*i,j*) for all grid points with -1 flag along with their corresponding normal coordinates x_n on the boundary. These data are stored in one-dimensional arrays. The forcing term of Eq. (2) is computed only on the forcing points so that the value of u_i^{n+1} on the forcing points projects the correct boundary condition on the x_n boundary points. Thus, the forcing term is equal to zero in every point of the computational domain apart from the grid points with -1 flag, where the forcing term is calculated by the equation:

$$f_i^{n+1} = \frac{V_{i\Psi} - u_i^n}{\Delta t} - H\left(u_i^n\right) - \frac{\partial P^{n+1}}{\partial x_i} \tag{8}$$

where $V_{i\Psi}$ is the imposed velocity of the immersed boundary. The computation consists of a bilinear interpolation where every variable φ in the fluid domain is associated with the values of the variable on the immersed boundary and its surrounding grid points 1-4 in the fluid domain (Fig. 3) using the expression:

$$\varphi_{fp} = \frac{h_2}{h_1 + h_2}\varphi_\Psi + \frac{h_1}{h_1 + h_2}\sum_{m=1}^{4}\alpha_m\varphi_m \tag{8}$$

where h_1 and h_2 are the corresponding distances (Fig. 3) and α_m are the bilinear interpolation constants.

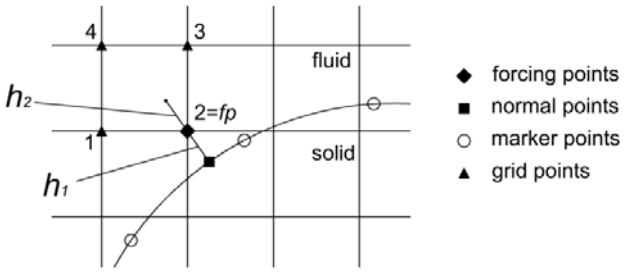

Figure 3. Association of flow variables on forcing points with flow variables on immersed interface and flow field grid points

Summing up, given the fact that all flow variables at time step *n* are known, the advancement to the next time-step follow these steps:

- Compute intermediate velocity by Eq. (4) imposing the pressure gradient of the oscillatory external flow and omitting the forcing term. These values do not satisfy the boundary conditions on the immersed boundary.
- Compute the term f_i^{n+1} at the forcing points by Eq. (8).
- Correct the intermediate velocity at the forcing points using the term f_i^{n+1}. These values satisfy the desired boundary conditions on the immersed boundary.
- Compute the dynamic pressure correction by Eq. (5) with appropriate boundary conditions on the computational domain boundaries but not on the immersed boundary.

- Update velocity and pressure by Eqs. (6) and (3), respectively.

2.3 Simulation set-up

The computational domain with the immersed ripple boundary is shown in Figure 2. The height of the computational domain is equal to the orbital motion amplitude plus the ripple height, its length is equal to one ripple length and the width (perpendicular to the left sketch) equals to two of the ripple height. The boundary conditions, for the solution of Poisson Eq. (5), were a zero Dirichlet condition at the bottom, zero Neumann condition (rigid-lid) at the top and periodic conditions in x and y directions.

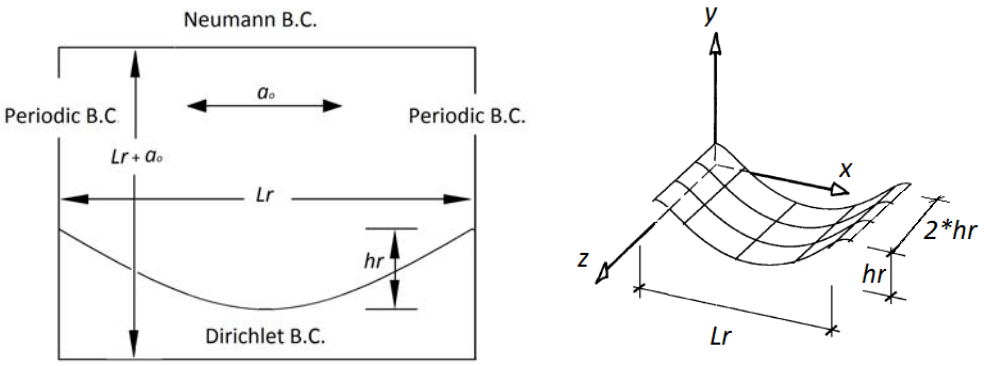

Figure 4. Sketches of the computational domain used in the simulations of oscillatory flow over a ripple

The grid spacing in x, y and z directions, $\Delta x/\alpha_o$, $\Delta y/\alpha_o$ and $\Delta z/\alpha_o$ are uniform and equal to 0.01. The flow is driven by a uniform pressure gradient at Reynolds number equal to 1250, based on the orbital motion amplitude $\alpha_o=U_o/\omega$, where U_o is the maximum velocity, $\omega=2\pi/T$ is the radial frequency and T is the period of the oscillatory flow.

Three cases of ripple characteristics were examined, according to the mobility number, ψ. According to [7] the mobility number, ψ, describes the ratio between the disturbing force and the stabilizing force due to gravity.

$$\psi = \frac{U_o^2}{(S-1)gD_g} \tag{9}$$

He also suggested that for sediments with densities close to that of quartz (S = 2.65), it is quite reasonable to describe ripple characteristics as a function of the mobility number. The ripple characteristics, which are the relative ripple length, L_r/α_o, and the relative ripple height, h_r/α_o, were determined according to [7] from Eq. (10), for three different values of the mobility number (ψ = 4, 10, 40), which cover a wide range of vortex ripples. The values calculated are presented in Table 1.

$$\frac{h_r}{a_o} = 0.275 - 0.0022 \times \psi^{0.5}$$
$$\frac{L_r}{a_o} = 2.2 - 0.345 \times \psi^{0.34} \tag{10}$$

ψ	L_r/α_o	h_r/α_o
4	1.647	0.231
10	1.445	0.205
40	0.991	0.136

Table 1: Ripple characteristics determined according to mobility number.

3 RESULTS

3.1 Model validation

To validate the accuracy of the computational model, three dimensional simulations have been conducted for oscillatory flow over a ripple and perpendicular to the ripple crestline with dimensions L_r = 1.33, h_r = 0.2, and

the numerical results were compared to previous numerical simulations. Good agreement is found when the present results are compared with those by [11]. Figure 5 presents the vorticity field at two time instants for Re = 1250.

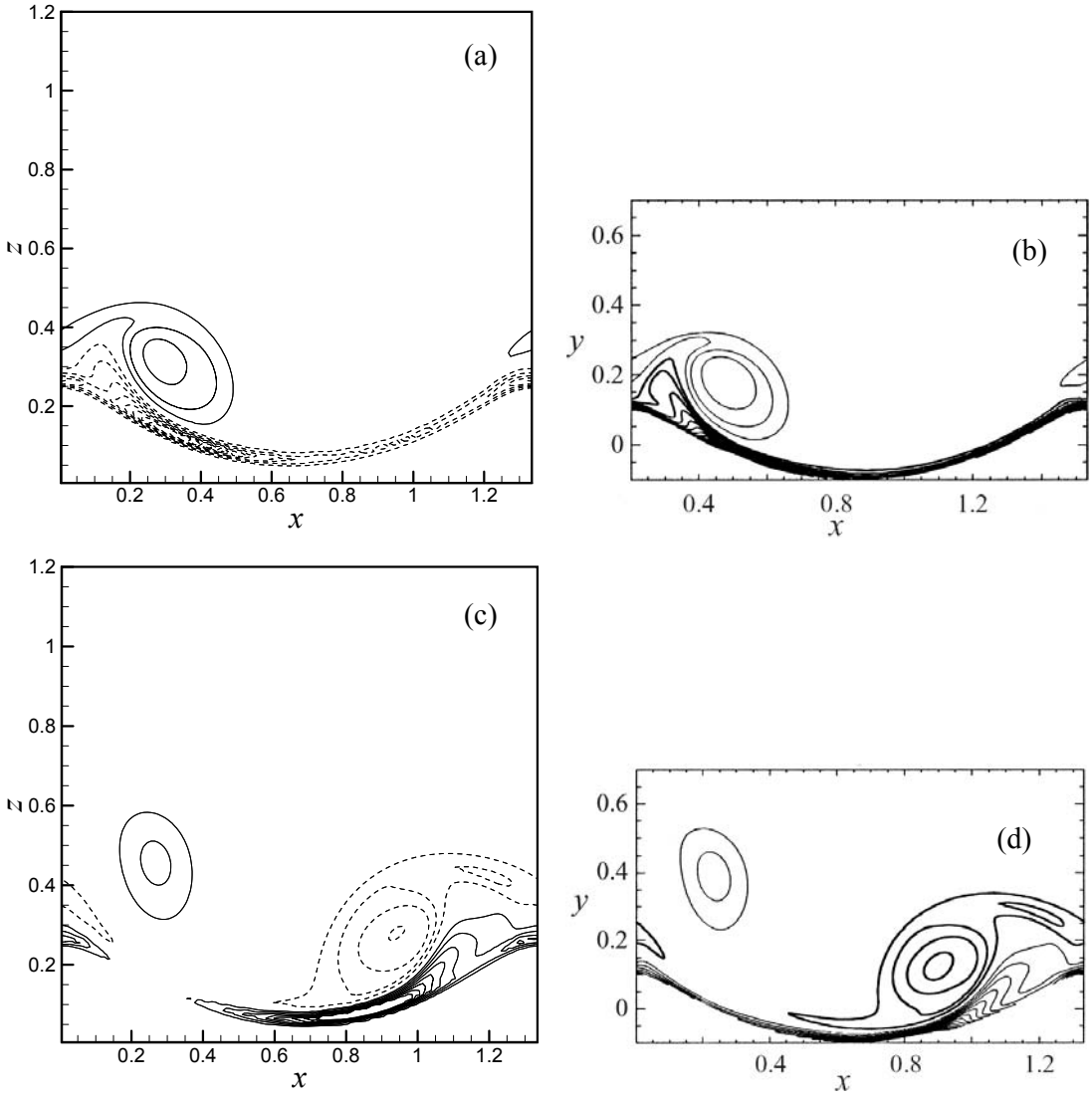

Figure 5. Spanwise vorticity, ω_y, for flow perpendicular to the ripple crestline (L_r = 1.33, h_r = 0.2, Re = 1250). Solid lines denote clockwise vorticity, while dashed lines anticlockwise. (a, b) $t = \pi$, (c, d) $t = 2\pi$, (a, c) 3-dimensional simulations, (b, d) Scandura et al. (2000).

Finally, Figure 6 illustrates the implementation of the IB method in a typical result. Specifically, the pressure field is shown along with velocity vectors, over a ripple, which is immersed in the Cartesian grid. The result shows that the numerically calculated boundary layer thickness is in accordance with the theoretical one

$$\delta = 4.6 * \delta_s = 4.6 * a_o \sqrt{\frac{2}{\mathrm{Re}}} \tag{9}$$

which yields δ = 0.184 for Re = 1250.

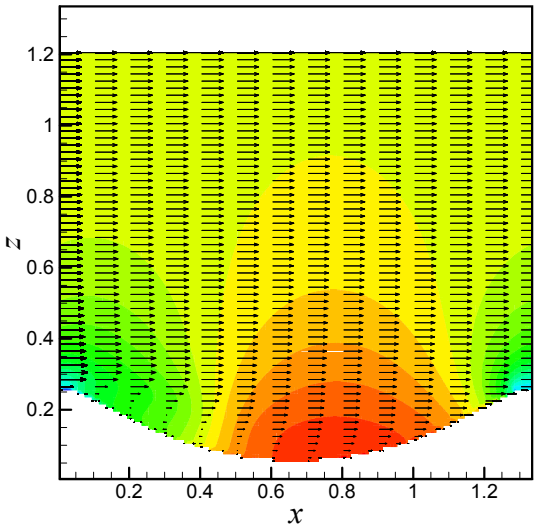

Figure 6. Pressure and velocity field over a ripple with $L_r = 1.33$, $h_r = 0.2$, for flow perpendicular to the ripple crestline. The satisfaction of the corresponding boundary conditions on the ripple surface is achieved by means of the IB method.

3.1 Three-dimensional results

Typical snapshots of the vorticity field over a ripple produced by flow perpendicular to the ripple crestline, are presented in Figure 7 and 8, for mobility number, $\psi = 10$ (which produces the steepest case with $L_r/h_r = 0.144$) and $Re = 1250$.

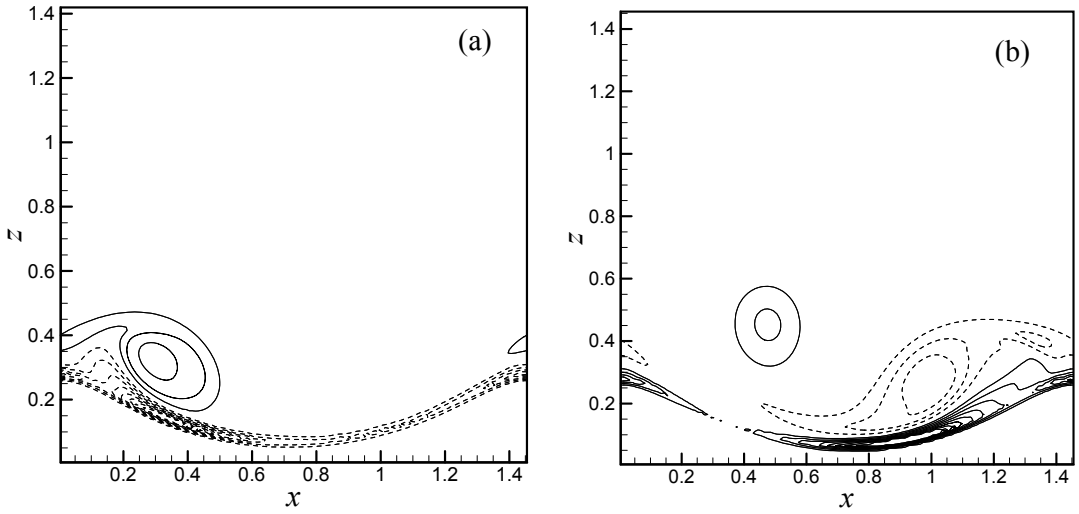

Figure 7. Vorticity field over a ripple with $L_r = 1.45$ and $h_r = 0.21$ ($\psi = 10$), for flow perpendicular to the ripple crestline. (a) $t = \pi$, (b) $t = 2\pi$

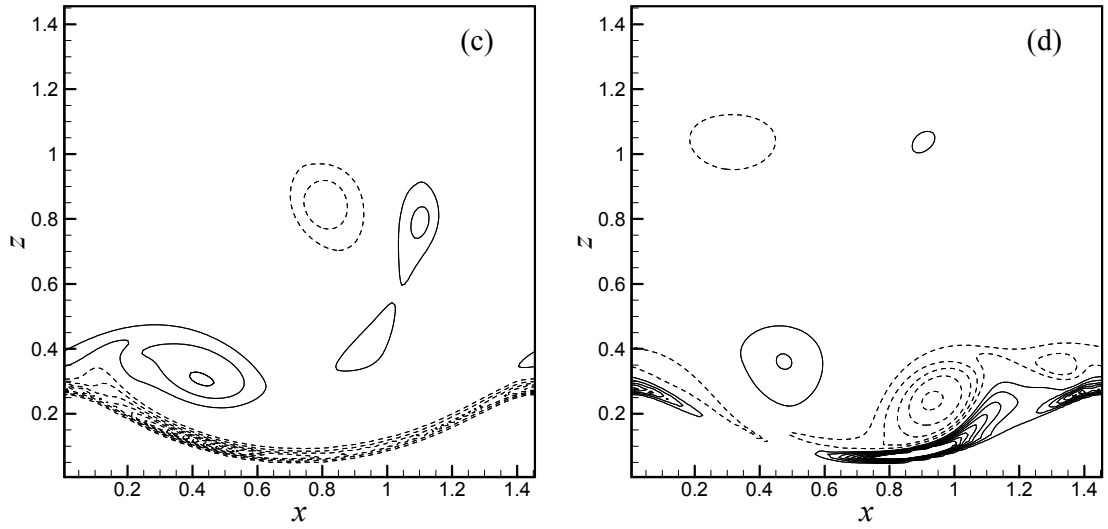

Figure 8. Vorticity field over a ripple with $L_r = 1.45$ and $h_r = 0.21$ ($\psi = 10$), for flow perpendicular to the ripple crestline. (c) $t = 3\pi$, (d) $t = 4\pi$

From Figures 7 and 8, it is clear that as the time passes, the oscillatory flow carries the vortices above the ripple. This is important because the sediment rise is correlated to the level reached by the vortices of the flow.

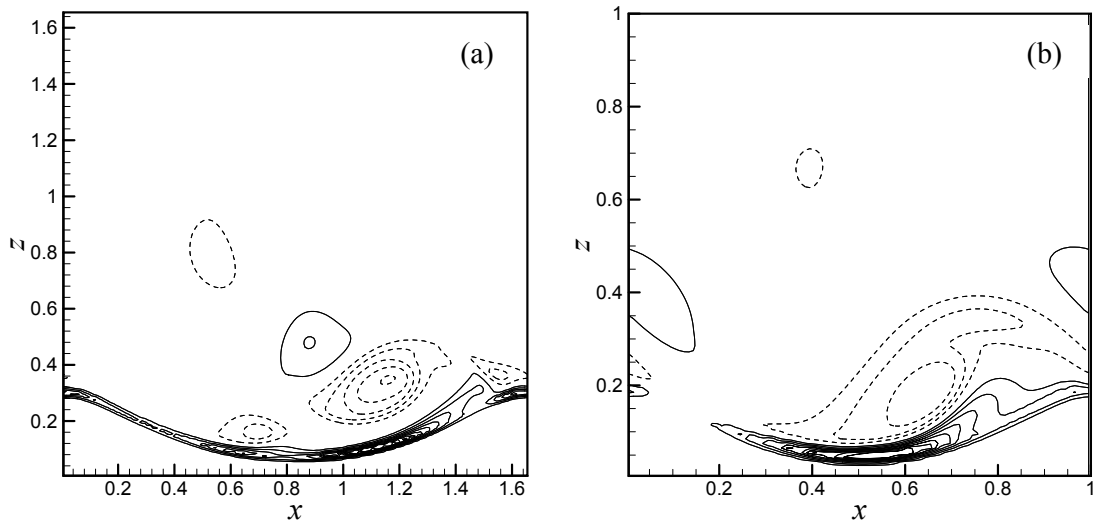

Figure 9. Vorticity field over a ripple at time step $t = 4\pi$, for flow perpendicular to the ripple crestline, (a) $\psi = 4$, (b) $\psi = 40$

Comparing Figure 8 (d) and Figure 9 (a, b), it is observed that the vortices are reaching higher levels as the dimensionless length of the ripple, L_r/a_o is increasing. In addition, stronger vortices are being created on these largest ripples.

The respective snapshots for oblique flow (at an angle of 45° to the ripple crestline) and with the same velocity magnitude and orbital motion amplitude, as the perpendicular flow, are presented at Figure 10. It is clear that due to the oblique flow (hence, smaller x-velocity component), the vortices are lower in height and in magnitude, comparing with the ones induced by the perpendicular flow.

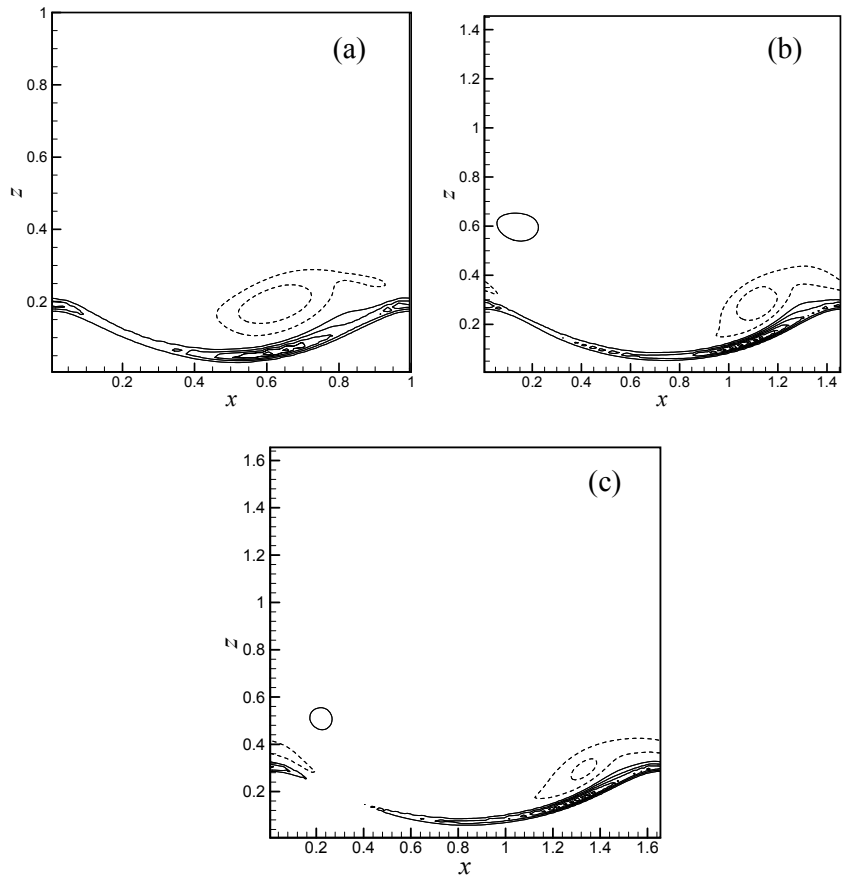

Figure 10. Vorticity field for time-step, $t = 4\pi$, for oblique flow (a) $\psi = 40$, (b) $\psi = 10$, (c) $\psi = 4$

Finally, we tried to reproduce the result of the oblique flow by simulating a perpendicular flow with $Re = 625$. The reason behind this selection (half the initial value of Reynolds number) is that the x-velocity component and the x-orbital motion component are both $1/\sqrt{2}$ of the ones for the oblique flow. However, by comparing, Figure 10 (a) and Figure 11, it is clear that the y-vorticity field is also affected by the y-velocity component, since for the oblique flow the vortices are a bit stronger than the perpendicular with $Re = 625$.

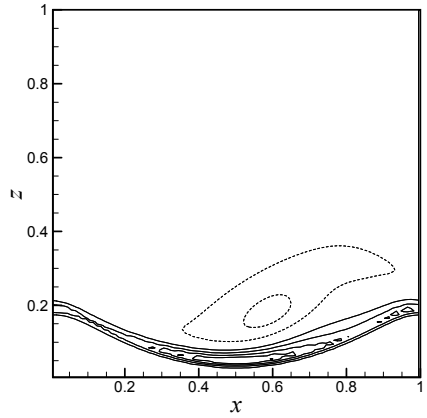

Figure 11. Vorticity field for time-step, for oblique flow, $\psi = 40$, $t = 4\pi$, $Re = 625$

4 CONCLUSIONS

Three dimensional simulations of perpendicular and oblique oscillatory flow were performed. The IB method was employed for the imposition of the ripple's geometry. It was found that the largest ripples produce the largest in height and magnitude vortices, while during the oblique flow simulations, the vortices were weaker. Finally, a perpendicular flow simulation with $Re = 625$ was performed in order to compare it, with the respective oblique one. The result was not the same, stressing that the y-velocity component produced by the oblique flow, is important on the formation of the vorticity field.

ACKNOWLEDGMENTS

This paper is part of the Initial Training Network SEDITRANS (GA number: 607394), implemented within the 7th Framework Programme of the European Commission under call FP7-PEOPLE-2013-ITN.

REFERENCES

[1] Al-Salem, A.A. (1993). *Sediment transport in oscillatory boundary layers under sheet flow conditions*. PhD Thesis, Delft University of Technology.

[2] Balaras, E., (2004). Modeling complex boundaries using an external force field on fixed Cartesian grids in large-eddy simulations. Computers & Fluids 375–404.

[3] Barr, B. C., Sinn, D. N., Pierro, T., and Winters, K. B. (2004). "Numerical simulation of turbulent, oscillatory flow over sand ripples." *Journal of Geophysical Research*, 109(C09009), 1–19.

[4] Intel Math Kernel Library, Reference Manual. MKL 11.0 Update 1.

[5] Malarkey, J., and Davies, A. G. (2004). "An eddy viscosity formulation for oscillatory flow over vortex ripples." *Journal of Geophysical Research*, 109 (C09016), 1–13. (C09016), 1–13.

[6] Nielsen, P. (1981). "Dynamics and geometry of wave-generated ripples.", *Journal of Geophysical Research*, 86(C7), 6467–6472.

[7] Nielsen, P., (1992). *Coastal Bottom Boundary Layers and Sediment Transport*. World Scientific, Singapore.

[8] O'Donoghue, T., Doucette, J. S., van der Werf, J. J., and Ribberink, J. S. (2006). "The dimensions of sand ripples in full-scale oscillatory flows." *Coastal Engineering*, 53(12), 997–1012.

[9] Peskin, C.S., (1972). "Flow patterns around heart valves: a numerical method." *Journal of Computational Physics*, 10(2), 252-271.

[10] Ribberink, J.S., and Al-Salem, A. A. (1994). "Sediment transport in oscillatory boundary layers in cases of rippled bed and sheet flow." *Journal of Geophysical Research*, 99, C6., 12707-12727.

[11] Scandura P., Vittori G., and Blondeaux P. (2000). "Three-dimensional oscillatory flow over steep ripples." *Journal Fluid Mechanics*, 412, 355-378.

[12] Werf van der, J. J., Ribberink, J. S., O' Donoghue, T., and Doucette, J. C. (2006). "Modelling and measurement of sand transport processes over full-scale ripples in oscillatory flow." *Coastal Engineering*, 53 (8), 657-673.

[13] Wiberg, P. L., and Harris, C. E. (1994). "Ripple geometry in wavedominated environments." *Journal of Geophysical Research,* 99(C1), 775–789.